JGR Space Physics

ADVANCING EARTH AND SPACE SCIENCE

Discovery of Alfvén Waves Planetward of Saturn's Rings

D. J. Southwood[1] , H. Cao[2] , O. Shebanits[1] , T. Elsden[3] , G. J. Hunt[1] , and M. K. Dougherty[1]

[1]Blackett Laboratory, Imperial College London, London, UK, [2]Department of Earth and Planetary Sciences, Harvard University, Cambridge, MA, USA, [3]School of Physics and Astronomy, University of Leicester, Leicester, UK

Abstract Between April and September 2017 in the final stages of the Cassini Saturn Orbiter mission the spacecraft executed 22 orbits passing planetward of the innermost ring, the D-ring. During all periapsis passes oscillations were detected in the azimuthal magnetic field components on typical time scales of a few minutes. We argue that these time-varying magnetic signals detected on the spacecraft are also primarily time-varying in the plasma frame. Furthermore, we show that nearly all signals exhibit a spatial feature, namely a magnetic node near the effective field line equator. We propose that the oscillations are associated with Alfvén waves excited in local field line resonances, most likely driven from global sources.

Plain Language Summary At the end of the Cassini Saturn Orbiter space mission, the spacecraft made multiple passes on the magnetic shells that pass planetward of the rings of Saturn. On each pass, Cassini recorded oscillations in the magnetic field, Alfvén waves. However, the waves appear to be likely to be driven at the natural frequencies of the whole magnetosphere. It is as if sound from a massive wind instrument is playing a celestial violin, namely the magnetic field lines in the small cavity below the rings.

1. Introduction

This study concerns oscillatory magnetic field measurements made during the final orbits of the Cassini spacecraft around Saturn where the spacecraft passed planetward of the D-ring at periapsis. We shall show strong evidence that the spacecraft passed through standing Alfvén wave structures on each pass while on magnetic shells planetward of the D-ring.

Remarkably, the magnetic signals obtained from April through to September 2017 during the proximal orbits show similar features from orbit to orbit despite large variations in the background azimuthal magnetic field recorded (Hunt et al., 2019; Provan et al., 2019). Strongly azimuthally polarized signals are found in two bands with time scales between 1 and 10 min which have a roughly harmonic relationship (periods ~150, 300 s) although precise spectral identification is limited as the spacecraft is planetward of the D-ring magnetic shells for only around 15 min during each orbit. Evidence is found that in both bands there is a magnetic node near the effective magnetic equator. This is the point where the background radial magnetic field component $B_r = 0$ and the field line is at its farthest from the center of the planet. In the simplest theoretical models, Alfvén wave eigenmodes would form field line resonances with standing structure along the field. Thus, wave fields would be symmetric or antisymmetric about that point. It is also suggested that the apparent observed magnetic field equatorial node indicates that the waves are pumped by global magnetospheric cavity resonances. The theory was first put forward by Kivelson and Southwood (1985). The ideas have been developed considerably and are now used in many terrestrial contexts (e.g., Bentley et al., 2018; Claudepierre et al., 2016; Elsden & Wright, 2019; Elsden et al., 2016; Takahashi et al., 2018; Wright & Elsden, 2016, 2020).

For all the proximal orbits (Rev 271–292 as well as the partial orbit [Rev 293]) periapsis is near midday. Orbits were highly inclined with the spacecraft passing from around 20°N–20°S while on shells crossing or within the D-ring. At the same time, the spacecraft typically passed through just under 2 h of local time (LT).

Figure 1 illustrates the spacecraft motion in radial distance, latitude and LT for the first and last full orbit (Rev 271 and Rev 292). The final dive-in trajectory, Rev 293, did not cross the ring plane, and is not included
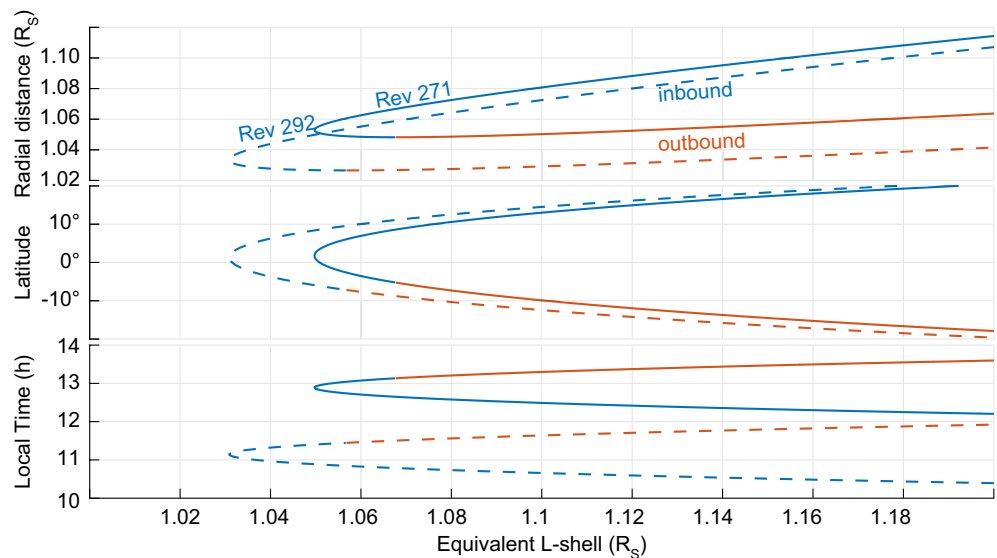
Figure 1. Spacecraft position coordinates versus magnetic shell labeling parameter, EqL, (top), planetary latitude (middle), and local time (bottom) for the first and last Cassini proximal orbits, Rev 271 (continuous) and Rev 292 (dashed). Traces are blue up to the closest approach to the planet and red afterward. The C11 internal Saturn field model (Dougherty et al., 2018) is used to compute the magnetic shell labeling parameter EqL, EqL (equivalent L shell) is the radial distance where a shell crosses the equatorial (ring) plane measured in Rs (Saturn radii). The model is axisymmetric and so shells are axisymmetric. On all orbits, Rev 271–292 inclusive, the innermost magnetic shell is encountered before periapsis, as is exemplified by the two traces in the top panel.

in this analysis. The x-axis in each plot in Figure 1 is the parameter we shall introduce to characterize magnetic shell, equivalent L shell (EqL). EqL is the distance where a shell crosses the equatorial (ring) plane measured in Saturn radii, Rs. It is derived from the most advanced internal planetary field model for Saturn (C11) (Dougherty et al., 2018). The field model is axisymmetric and so magnetic shells are axisymmetric. The 20 other passes have a LT profile between the two shown and similar latitude coverage. Blue and red traces indicate where the spacecraft is moving radially inbound and outbound respectively. The innermost shell penetration varies between EqL values of 1.03 and 1.06 during the proximal orbits. The top panel in Figure 1 makes clear that the points where spacecraft is at its minimum radial distance are well separated from where it encounters the innermost magnetic shell. This is not only because the orbit is not symmetric north-south but also because the magnetic field itself is not north-south symmetric. This latter point will be important later in the study.

For much of what we shall discuss whether the spacecraft is moving inward or outward across magnetic shells is what is important. Accordingly, in what follows we shall regard the spacecraft as moving inbound until it encounters the innermost magnetic shell and outbound afterward.

While the spacecraft was on magnetic shells mapping to within the D-ring inner radius, (EqL < 1.11), large and unexpected azimuthal magnetic perturbations were discovered. Dougherty et al. (2018) and Khurana et al. (2018) reported strong large scale changes in the azimuthal magnetic field (B_ϕ) of magnitude up to 20–30 nT and predominantly in the sense of planetary rotation during the early proximal orbits.

In Figure 2 we show an example of departures from the C11 model planetary field magnetic field during the first proximal orbit (Rev 271). The shaded region shows where the spacecraft is crossing magnetic shells within the D-ring. Spherical polar components of the field are plotted. Although small departures are seen in the radial and theta field, the B_ϕ changes stand out.

The raw data used in the figure have a time resolution of 1 s. The fuzzy nature of the traces is due to digitization noise. The spacecraft magnetometer is operating in a background field of magnitude ~16 μT. As did Provan et al. (2019), we smooth the data by using 1 min running averages of the data henceforth. The result is the blue traces overlaid in all three panels of Figure 2. Henceforth we use the 1 min running average as the basis for study.
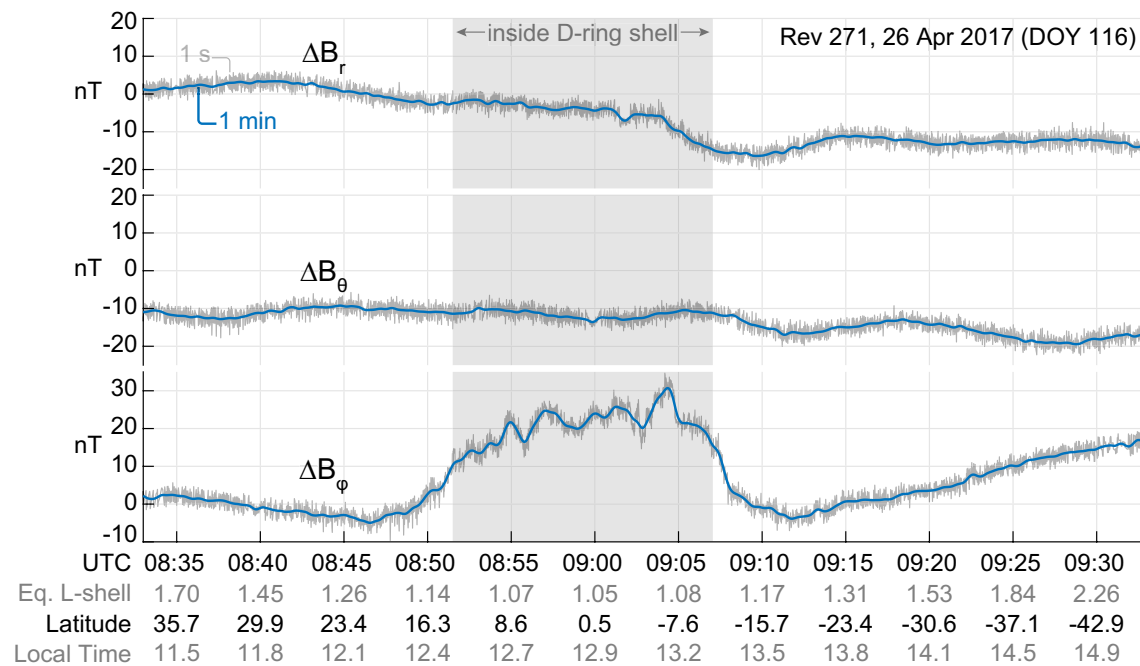
Figure 2. Three components of the magnetic field (units nT) in planet-centered spherical polar coordinates on the first of the Cassini proximal orbits. The model C11 field has been subtracted from the measured field to provide the traces, ΔB_r and ΔB_θ, shown in the top two panels. The gray traces show 1 s time resolution. Digitization noise is evident on short times scales and 1 min running averages (blue traces) are used for all subsequent plots in the study. The data are plotted against time on April 26, 2017 (Day 116). The ancillary data shown below the time axis are: EqL, (equivalent L shell) magnetic shell parameter, Spacecraft Latitude (deg) and Local Time (hours).

Khurana et al. (2018) proposed an explanation for the large eastward magnetic perturbation shown in the bottom panel of Figure 2. Given the local strong southward background planetary field, the sense of the B_ϕ perturbation (in the direction of planetary rotation) originally reported was consistent with there being a net interhemispheric Maxwell magnetic stress corresponding to the southern ionosphere dragging the northern in the prograde (eastward) sense. The sense of asymmetry was unexpected in northern summer when compared to the Earth's magnetic field as field line tying in the equivalent E region ionosphere is then expected to be stronger in the north in that season. However, Khurana et al. (2018) pointed out that if a significant fraction of the speed of the 1-bar level atmospheric equatorial jet were sustained to thermospheric heights, the northward offset of the planetary dipole field (due to the axial quadrupole) would lead to such a B_ϕ signature. Any asymmetry in ionospheric conductivity could further modulate the amplitude of the signal but will not change the sign of B_ϕ (e.g., see Equation A8 in Provan et al., 2019).

Provan et al. (2019) classified passes into four categories, A, B, C, and U according to the shape of the background B_ϕ perturbation detected as the spacecraft crossed the magnetic shells mapping planetward of the D-ring. For category A, the azimuthal field component B_ϕ rises as the spacecraft passes across the D-ring field lines to come to a single fairly central positive peak value near the point where the innermost magnetic shell is met. The overall amplitude is typically ~20–40 nT. As the spacecraft moves back out toward the D-ring magnetic shells B_ϕ decreases with the overall disturbance looking close to symmetric about the point where the spacecraft encounters the innermost shell.

In category B, B_ϕ is similarly symmetric between inbound and outbound orbital legs with peak amplitude typically ~10–20 nT. However, the overall shape is different being double or triple peaked where the outer two peak amplitudes are found near or just planetward of the shell corresponding to the boundary of the inner D-ring. On the shells inward of the two outer peaks, B_ϕ either dips to a minimum near the innermost shell or first dips and then rebounds to another peak near the innermost shell. Categories A and B account for around 55% of the proximal passes. Of the remaining passes, Category C (3 cases) features a positive B_ϕ peak on the innermost shells but the symmetry about the innermost shell is lost. The final Category is
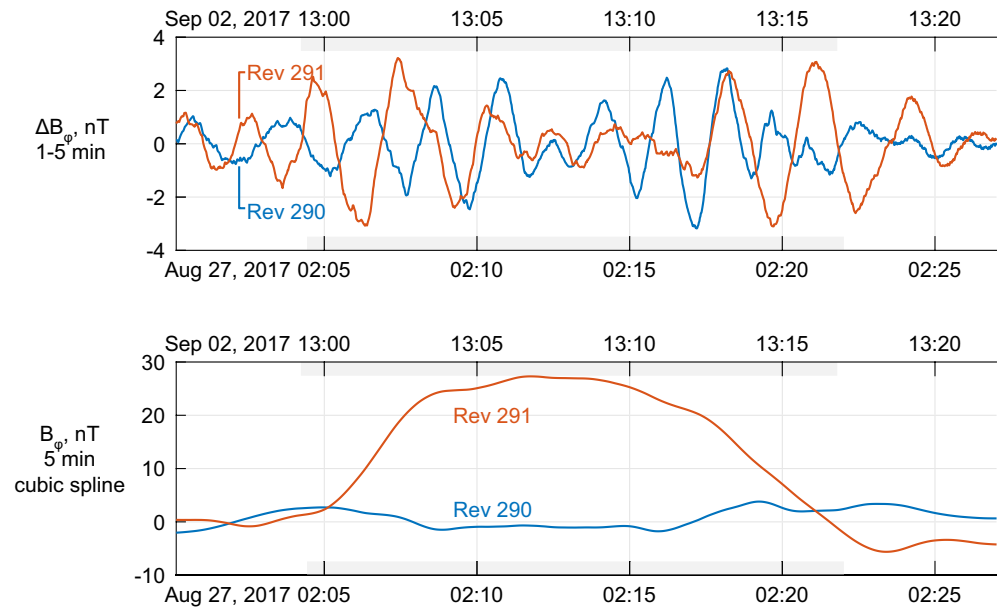
Figure 3. Azimuthal field data from periapsis passes of Revs 291 (red traces) and 290 (blue traces). The time axis for Rev 291 on Day 245 of 2017 is above each panel. The time axis for Rev 290 data is below. The time shift between axes is 557,687 s (6.4547 days) chosen to align the times of crossing the innermost magnetic shell, EqL = 1.03. The data in the top panels have been derived by subtracting a cubic spline with a 5 min running window fitted to smoothed 1s resolution data. The process effectively filters the data. The bottom panel shows the spline, effectively the background low pass data. The two adjacent orbits illustrate the similarity of the high frequency signals with contrasting background signals. The background signal on Rev 291 is the most common A category while Rev 290 illustrates the uncommon category U as classified by Provan et al. (2019).

designated U; the 5 passes are each unique in resisting fit to the previous categories. There are two cases where the predominant perturbation is large and negative.

The time taken between crossings of the outer D-ring magnetic shells on each orbit is of order 25 min (1,500 s) and the time on each proximal orbit when Cassini was planetward of the D-ring magnetic shells is about 15 min (900 s). We focus on oscillatory signals with time scales less than 10 min (600 s). As a by-product of our analysis procedure we produce polynomial fits to the B_ϕ signature encountered on each pass smoothed by 10-min windowing. On most passes, the resulting smoothed signature of five of the seven Category B signatures resembles Category A. Rev 277 still reveals a central local minimum as in Category B, while Rev 288 shows very little background perturbation at all and would thus be Category U.

Overall, we conclude that the majority of the oscillations seen in this study take place against a background positive B_ϕ with amplitude varying from orbit to orbit. The symmetry in the background B_ϕ about the equator implies that they represent momentum transport from south to north (as proposed by Khurana et al., 2018). Our smoothed plots superposed for all complete orbits (Revs 271–292) appear later in the study in the lowest panel of Figure 5. Two exceptional cases are noted by Provan et al. (2019) where B_ϕ exhibits a large overall negative deviation. In these cases, the interhemispheric electromagnetic stress is reversed with the implication that the north-south difference in thermospheric flow in the theory of Khurana et al. (2018) would be reversed. We shall not investigate this issue further here.

2. Observations of Azimuthal Magnetic Oscillations

A first assumption might be that the background B_ϕ perturbation might in some way be the source of the oscillatory signals detected. We shall conclude in the end that this is not so. Our first evidence concerns the similarity of the oscillatory signals from orbit to orbit while the background B_ϕ is very different. On all passes, we have separated oscillatory signals from a background by subtracting a cubic spline with window-
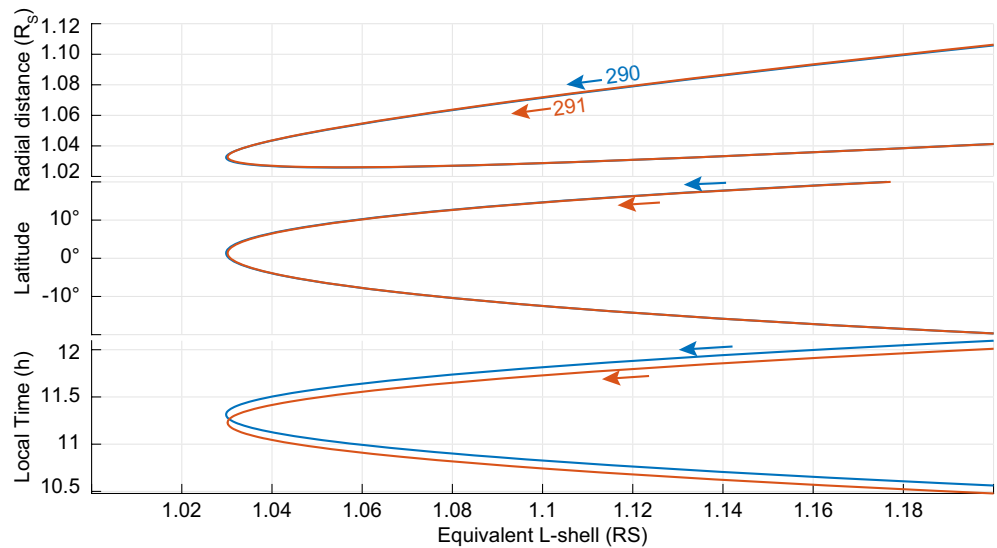
Figure 4. Spacecraft trajectory information for Rev 290 (blue) and Rev 291 (red). Radial distance, latitude and local time (LT) are plotted versus EqL. Arrows indicate the direction of travel. The latitude and radial distance traces for the two orbits are indistinguishable on the scale shown.

ing chosen to be shorter than the time scale (~15–25 min) of the passage. The remaining signal yields the oscillatory signals. The spline provides a smoothed background.

In Figure 3, we illustrate how our procedure to separate oscillations from background in the Cassini magnetometer data works for two consecutive periapsis passes, Rev 290 and Rev 291. Twenty four minutes of data from the two passes are shown. The time axis shows the recorded time for Rev 291. Rev 291 data are the red traces. The time axis for Rev 291 is above each panel. Rev 290 data are blue. The time axis is below each panel. The difference between times is 6.4547 days (6 days 10 h 55 min) so that times of crossing the innermost magnetic shell are aligned. The spacecraft trajectories are almost identical except for a slight shift in LT as shown in Figure 4. Data shown in Figure 3 begin and end when the spacecraft crosses the magnetic shell mapping to the outer edge of the D-ring based on the C11 model (Dougherty et al., 2018).

The data in Figure 3 are obtained by applying a cubic spline fit with a 5 min window to the 1 min running average data. The resulting smoothed splines from each pass are shown in the lower panel in Figure 3. The upper panel shows the residual signal found by subtracting the spline from the original 1 min running averaged 1 s data.

A few words on the procedure chosen are appropriate. Our method means that by adding data plotted in each trace in the lower panel to the data for the appropriate trace in the upper panel, one may reconstruct the 1 min running average data. Nonetheless, use of the spline fit resembles using low and high pass filters to divide the signal. Given the short time where the spacecraft is in the domain where signals are present it does not make sense to Fourier transform and work in the spectral domain. We shall refer to the resulting data with 5 min windowed cubic spline subtracted as being in the 1–5 min band. The labels of the y-axis of the top panel of Figure 3 use this nomenclature. In both panels the Rev 290 trace is blue and Rev 291 is the red trace. Given the relatively short time scale of the passage within the D-ring shells, the use of more precise filtering does not seem sensible. Later in the study we shall apply the procedure several times, calculating splines with changing window width, to provide a multiband view.

The red and blue traces in the lower panel of Figure 3 are very different. The Rev 291 trace provides an example of Provan et al.'s category A pass. There are eight such passes in the proximal orbit set. Provan et al. describes the category A azimuthal field perturbation rising from the baseline inbound to a single principal peak centered near the field parallel point (i.e., innermost magnetic shell), before declining nearly symmetrically back to the main ring region baseline outbound. The smoothed trace from the spline fitting
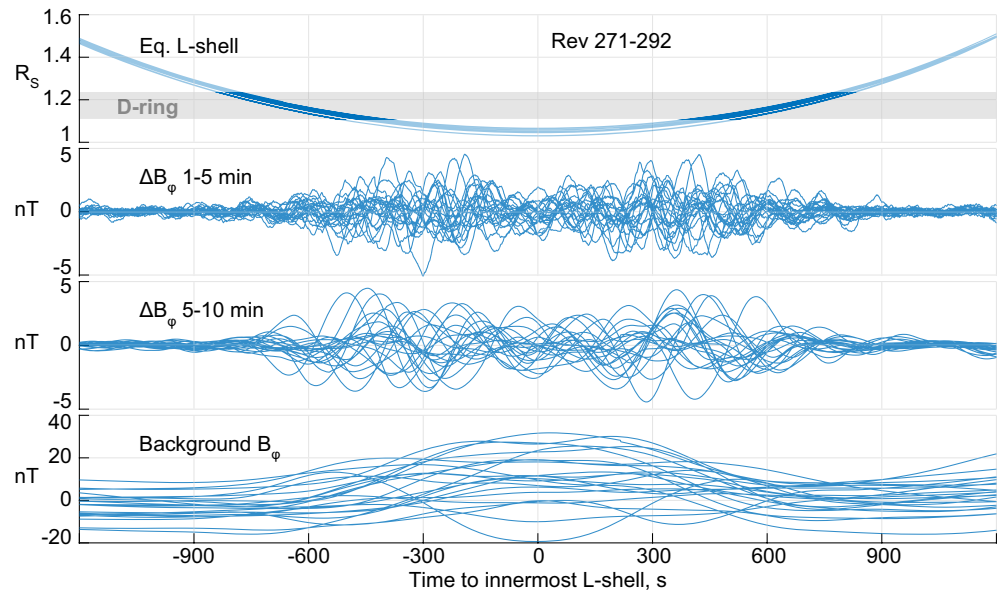
Figure 5. The three lower panels show azimuthal magnetic field filtered into bands using the process described in the text for all 22 proximal orbits. The origin for the x-axis of all panels is time from the spacecraft encounter with the innermost magnetic shell (i.e., lowest EqL). The top panel shows overlaid the magnetic shell position; the crossing of the D-ring magnetic shells is shaded. On the scale of the plot the orbits are barely distinguishable. Units for magnetic data are nT.

reflects this. Rev 290 is a category U pass. It stands out as the pass with the lowest overall variation in background B_ϕ.

Plots of spacecraft position coordinates for the two periapsis passes (Rev 290 and 291) are shown in Figure 4. Radial distance, latitude and LT are plotted against magnetic shell parameter (EqL) for both orbits. Spacecraft were below EqL = 1.2 between 02:01:56 and 02:25:45 on Day 238 (Rev 290) and from 12:57:44 to 13:20:32 on Day 245 (Rev 291). The radial distance and latitude are indistinguishable on the scale shown. Where the spacecraft was on a magnetic shell with EqL < 1.24, that is, planetward of the outermost shell crossing the D-ring, the latitude varied from ∼17° to −21° for both orbits while the LT varied from 10.6 to 12.0 h (Rev 290) and 10.7 to 12.1 h (Rev 291) (i.e., ∼6 min difference). The deepest penetration of the planetary field, are, respectively, EqL = 1.0299 (Rev 290) and EqL = 1.0303 (Rev 291). The radial distance from the planet, latitude and LT at these times are $1.0324R_S$, 1.32°, 11.31 h (Rev 290), and $1.03255R_S$, 1.21°, 11.23 h (Rev 291). The similarity of the orbits in Sun-fixed coordinates implies that the differences between passes are likely to be due to time variation between orbits rather than any inherent LT variation.

Despite the large difference evident in the background azimuthal field for each pass, the traces for the 1–5 min band-limited signals in the upper panel of Figure 3 are similar. Such irregular oscillations with varying amplitude are recorded by the spacecraft on a time scale of minutes with amplitudes of 2–5 nT on all proximal periapsis passes.

The use of 5 min for windowing the spline fit is not enough to remove all oscillations. Small amplitude oscillations on a longer time scale are perceptible in the background field plots in the bottom panel of Figure 3. The time scales of these additional oscillations in the spacecraft frame are between 5 and 10 min. A further use of a windowed cubic spline fit but with a 10 min window resulted in the superposed plots illustrated in Figure 5. The x-axis in each plot is time in seconds where $t = 0$ is measured from when the spacecraft crosses the innermost magnetic shell. Each panel shows data overlaid from all 22 proximal orbits when the spacecraft was on flux tubes with EqL < 2. The top panel shows the spacecraft magnetic shell parameter (EqL). Horizontal shading indicates where the spacecraft is crossing the D-ring magnetic shells.

The data in Figure 5 are split into three bands derived in the following manner. The second panel with y-axis labeled 1–5 min shows data derived in the same way as in Figure 3. The third panel, labeled 5–10 min, is
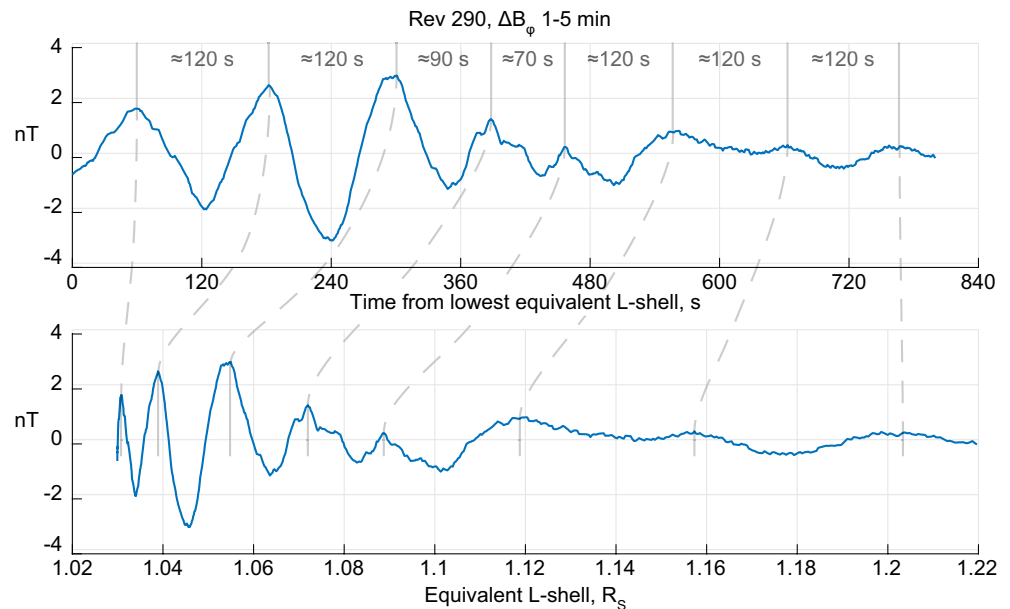
Figure 6. The azimuthal magnetic signal from the 1–5 min band from the outbound pass of Rev 290 plotted versus time in the top panel and the EqL magnetic shell variable in the bottom. Dashed lines link the peaks in each panel. Times between peaks in amplitude are shown in the top panel.

the residual signal left after a cubic spline fit with a 10 min window has been applied on the residual 5 min window spline. The resulting spline with a 10 min window is shown in the bottom panel.

The variety of profiles that the central B_ϕ perturbation can take and that were classified by Provan et al. (2019) are evident in the bottom panel. We shall concentrate attention on the data plotted in the middle two panels.

The division of the residual data after subtraction of the background spline into two bands is significant. The signals in the 1–5 and 5–10 min bands are of remarkably similar peak amplitude (typically ≤ 4 nT). The signal amplitudes in both bands appear smaller where the spacecraft is near the innermost L shell and largest just planetward of the magnetic shell of the D-ring inner edge. Although signals may be present beyond the D-ring, amplitudes are much reduced.

3. Space versus Time Dependence

The signals are detected as a time series by the spacecraft but, of course, part of the variation seen may be due to the spacecraft moving through static or slowly varying spatial structures, ordered by magnetic shell or in latitude. As noted earlier, the Khurana et al. (2018) theory assumes that the time variation detected in the background B_ϕ is due to the spacecraft motion through a quasistatic structure, as does the field aligned current analysis of Hunt et al. (2019).

We shall assume that the oscillations detected on time scales <10 min are not primarily due to the spacecraft radial motion. Some assurance that the assumption is reasonable is illustrated in Figure 6.

In the upper panel of Figure 6 we show the residual ΔB_ϕ time series signal in the 1–5 min band from the outbound pass of Rev 290. Dashed lines link the peaks in the trace in each panel; the time separation between peaks is also given in the upper panel. In the lower panel the same data is plotted versus equivalent L shell. Although the oscillations in the upper plot are not sinusoidal, they are more regularly spaced than in the lower. For all passes this is true and in a few cases the signal can even appear close to sinusoidal as a function of time throughout.

In Figure 7 we show an example of close to sinusoidal signals from Rev 292. Because in this case one period appears close to 5 min, the boundary between high and low frequency bands was modified to 4 min. There
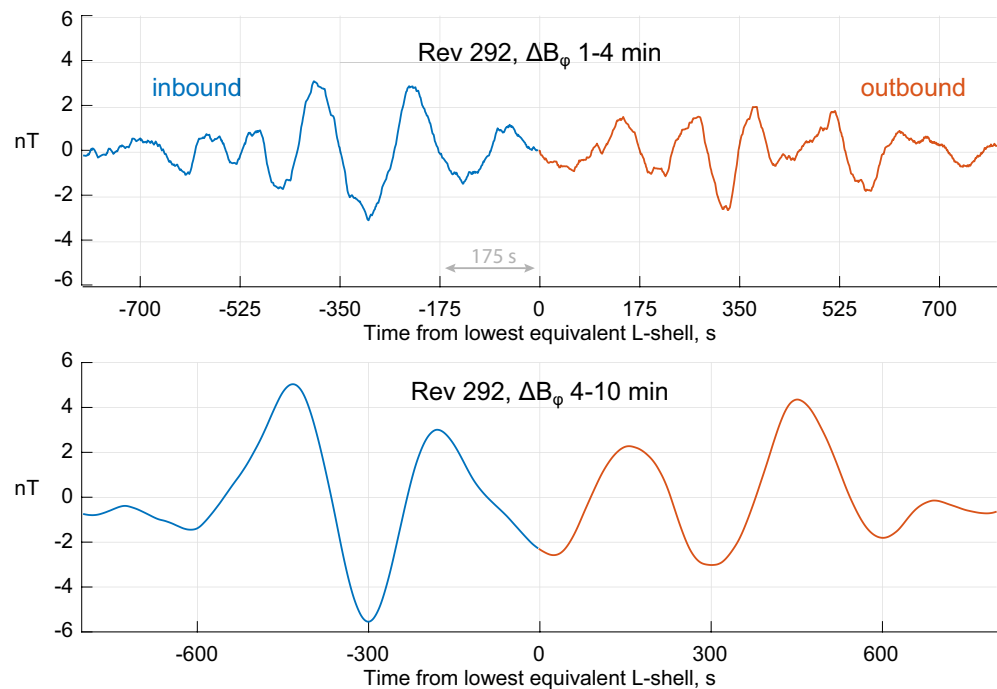
Figure 7. Sinusoidal signals in B_ϕ on Rev 292. The signal has been divided into 1–4 min band (upper panel) and 4–10 min band (lower panel). Inbound trace is shown blue, outbound, red. The x-axis in each panel is time, T, measured with respect to the innermost magnetic shell crossing (EqL = 1.03). There is a vertical grid spacing of every 175 s (upper panel) and every 300 s (lower panel).

was a marginal increase in amplitude in the longer time scale band due to this change. The upper panel shows the high frequency band and the lower the low frequency band. The signals in each panel are plotted against time, T, measured from where the spacecraft encounters the innermost magnetic shell (EqL = 1.03). The inbound trace is blue, outbound, red. In the 1,600 s (26m 40s) of data shown, the spacecraft moved from EqL = 1.22 in and back out to EqL = 1.22, just short of the magnetic shell at the outer edge of the D-ring. The magnetic shell at the D-ring inner edge at EqL = 1.11 is crossed near T = ±525 s.

In the upper panel gray vertical markers are placed at 175 s intervals (~3 min). In the lower panel vertical markers are placed at 300 s (5 min) intervals. In the lower panel the vertical markers well approximate the positions of five troughs. In the upper panel, the 175 s markers pick out the majority of the zeroes. This is better than chance but there are sharp changes in phase and there are signals that might be at a higher frequency present at certain points in the upper panel, for example, at around T = −500 s and 400 s.

Recalling that the signal recorded by the spacecraft can be reconstituted by adding the signals in the two panels to the smooth background cubic spline with 10 min window, Figure 7 argues strongly that the oscillatory signals encountered are made up of two near sinusoidal frequencies along this orbit.

One can process other passes similarly to seek quasisinusoidal behavior. Few show a structure as simple as Rev 292. A more complex example is shown in Figure 8 from Rev 278, a pass where the background in the bottom panel is classified as category C by Provan et al. (2019). Once again data are plotted against time measured from the time that the spacecraft encountered the innermost magnetic shell or lowest equivalent L shell, EqL.

For this pass the shortest time variation signals in the top panel were derived by subtracting a cubic spline with a 3 min window. The spline derived from that process was then fitted with a 5 min window cubic spline to give the second panel. In the third panel a further spline with 10 min window has been subtracted. We label the y-axis, 1–3, 3–5, and 5–10 min indicating the windows used for each panel. The residual data, the spline with 10 min window, the background, is then displayed in the fourth panel.
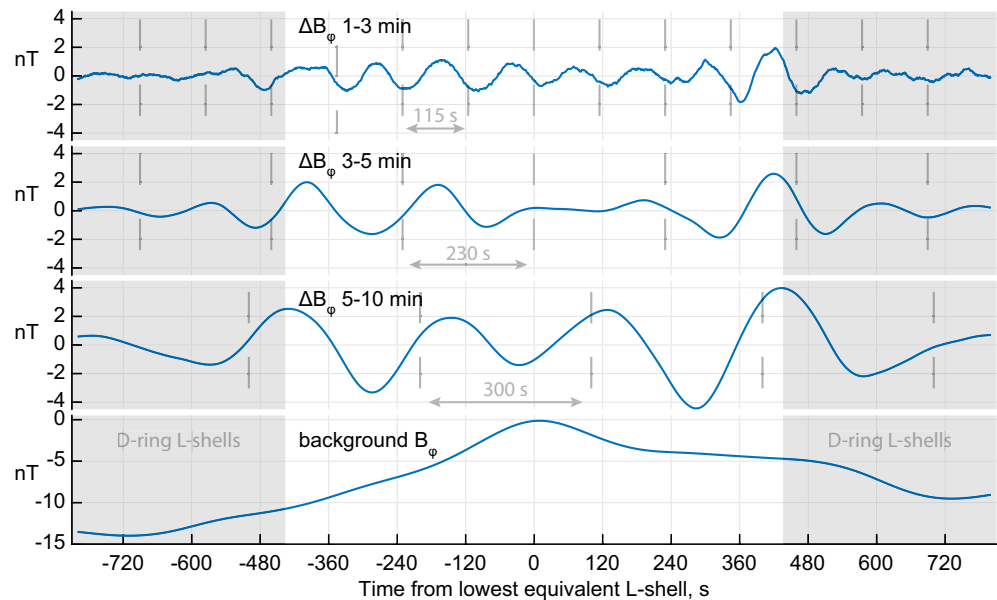
Figure 8. Azimuthal field B_ϕ from Rev 278 divided into four bands (1–3 min, 3–5 min, 5–10 min, background) obtained by windowing as described in the text. Time is measured from the time of encountering the innermost magnetic shell. Where the spacecraft is on D-ring shells is shaded. Dashed markers in the top three panels are separated by 115 s, 230 s and 300 s respectively. Each panel is labeled to indicate the windowing used for the band displayed.

To aid the eye, vertical markers are spaced at 115 s in the top panel and 230 s and 300 s in the next two panels respectively. Both plots show evidence of sinusoidal signals but in the 3–5 min band there is a phase shift between left and right-hand sides. In the third panel, although the amplitude is variable, the 300 s markers match well the period apparent in three cycles of the signal in the panel. However, again, the phase matching breaks down between the left and right-hand side of the plot. The markers line up with zeroes on the left but shift to closer to the peak on the right. A possible explanation of this effect will be given in the next section.

The signals are spatially limited within a bounding shell passing somewhere near the D-ring inner edge. In the next section we shall introduce various other causes of spatial structure giving rise to a Doppler shift because of the spacecraft motion. However, we shall continue to assume as a basis that, in large measure, the oscillatory signals detected by the spacecraft are not set up by the spacecraft moving through spatial structure but are time varying in the plasma frame.

4. Theory: Standing Alfvén Mode

In any system where boundaries are reflecting the lowest frequency oscillatory signals are likely to be standing eigenmodes. In a cold magnetized plasma, there are two low frequency modes in a uniform plasma, the fast isotropic mode and the field-guided Alfvén or transverse mode. The signals shown in this study are in the azimuthal field, ΔB_ϕ, transverse to the background field, which during the events has a magnitude between 13 and 16 µT.

The ΔB_ϕ amplitudes in the events considered here exceed the amplitudes on similar time scales in the other components by up to an order of magnitude. The B_ϕ oscillations are close to transverse to the background field and it is reasonable to start by considering the signals as in the Alfvén mode and guided by the background magnetic field. Field lines in this mode behave like oscillating strings. Waves are reflected at the northern and southern ends of the flux tube in the ionosphere. The field lines can go into resonance resulting in signals standing along the field. The eigenfrequencies depend only on how the system varies along the background field and so they vary from magnetic shell to shell. If the signals have a standing mode
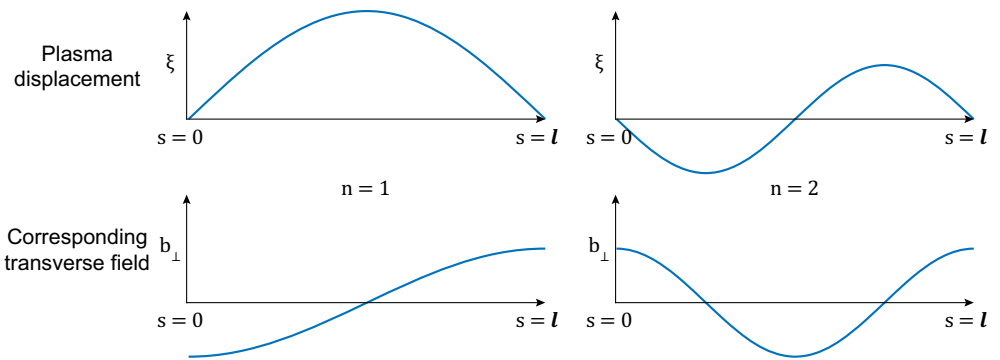
Figure 9. Form of eigenmodes in a straight field and a uniform plasma. The upper sketches show the plasma displacement, ξ, for the first two harmonics. s is the distance along the field. Perfect reflection (with $\xi = 0$) is assumed at the ionospheric boundaries at $s = 0$ and l. The lower panels show transverse magnetic field ($b_\perp$) for the same harmonics. The $n = 1$ mode has a node in the transverse field at the mid-point, that is, the equator, assuming N-S symmetry in the background. The $n = 2$ mode has a field antinode.

structure along the magnetic flux tubes with similar reflection at the ionospheres, there will be either a node or an antinode at the equator.

The sketches in Figure 9 illustrate schematically the form of eigenmodes. The field line is notionally straightened out and the upper sketches show the form of the plasma displacement, ξ, for the first two harmonics. s is the distance along the field. Perfect reflection (with $\xi = 0$) is assumed at the ionospheric boundaries at $s = 0$ and l. The lower panels show the form of the transverse magnetic field ($b_\perp$). The $n = 1$ mode has a node in the transverse field at the mid-point, i.e. the equator, assuming N-S symmetry in the background.
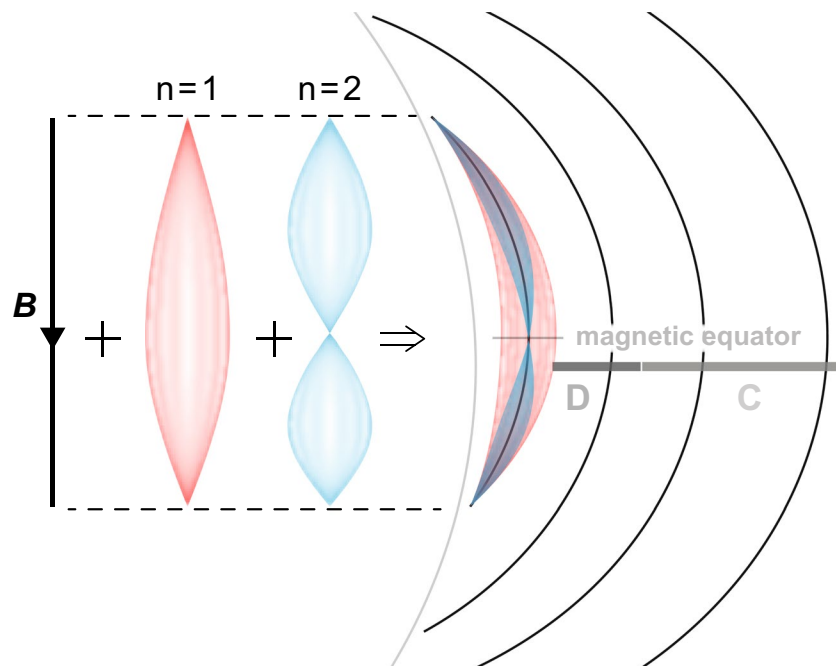
Figure 10. A composite sketch showing the lowest frequency standing modes scaled for field lines planetward of the D-ring and scaled also to represent the north-south asymmetry in the planetary field. Proportions are appropriate for the C11 field model. On the left is a schematic of idealized $n = 1$ and $n = 2$ eigenmode structure. On the right, the displacement of the field in the eigenmodes is shown in the more realistic geometry with the field lines anchored at 1000 km above the 1 bar level. Although sketched as if motion is in the radial direction, in fact the motion in the eigenmodes is azimuthal. The D and C rings are shown. The proxy magnetic equator is north of the ring plane.

The $n = 2$ mode has a field antinode. All odd n modes have an equatorial node in the field whereas even n modes have an antinode at the equator.

Figure 10 illustrates the oscillating field lines sketched to scale with respect to the planet. The field line is straightened out in the sketch inset on the left-hand side and the $n = 1$ and 2 standing structures are shown. However, these have been drawn proportional to the scale of the planetary outline (illustrated by the gray curve). The effective magnetic equator (the location of the most distant point from the planet of the undisturbed field line) is also drawn to scale using the C11 Saturn field model as the guide. It is assumed that the location of an antinode for field line displacement for $n = 1$ and field displacement node for $n = 2$ would be located near this point.

On the right of the figure beyond the curve representing the planet, the $n = 1$ (red) and 2 (blue) torsional field displacements are sketched to illustrate how the waves would fit into the region below the D-ring. Although the 2-D sketch could make it appear as if motion is in the radial direction, the motion in the eigenmodes discussed here is azimuthal. The outermost field line of the cavity planetward of the D-ring roughly bounds the region where the signals are seen. A line indicates the presence of the D and C planetary rings beyond this radius.

The sketches in Figures 9 and 10 are based on assuming perfect reflection of the signal by highly conducting E-region ionospheric boundaries in which the field line feet are effectively anchored. Any asymmetry in the conductivity and reflectivity at the field line feet will remove the precise symmetry. The antinodes and nodes evident at the mid-point (s = $l/2$) in the sketch will be moved from the mid-point toward the weaker reflecting ionosphere.

When a signal has a node at the equator, an observer moving through the equator will normally see a change of sign of the field whatever the phase of the signal is in the time domain. An exception is if the time domain phase is also zero. Then the signal at the equator would still be zero but the field will exhibit a local minimum there. In either case, the moving observer would detect an apparent phase skip in the signal. This effect may well explain the phase shift seen between left and right-hand sides of panel 3 in Figure 8. We discuss the observable effects of standing structure and nodes in the next section.

5. Standing Structure in the Observations?

In Figure 7, at first glance it looks in the two plots as if there is a magnetic antinode (signal peak) in the low frequency signal at T = 0 and a node (signal zero) in the high frequency. This is almost certainly fortuitous as the point on the orbit where the spacecraft encounters the innermost shell is not at either the planetary equator or what might be regarded as the magnetic field equator at that time. The Saturn field is axisymmetric with respect to the rotation axis, but it is not north-south symmetric. Even the dipole component is shifted substantially toward the north along the rotation axis (Cao et al., 2019; Dougherty et al., 2018). When a magnetic shell is most distant from the planetary surface, the radial component should change sign. We shall refer to the point on the orbit where the condition $B_r = 0$ as the proxy magnetic equator.

On Rev 292, the proxy equator where $B_r = 0$ occurs at T = −100 s before the innermost shell encounter on the inbound pass. Inspection of Figure 7 shows that there are points in both panels where $\Delta B_\phi = 0$ near T = −100 s. The nodes occur precisely at T = −92 s top panel T = −100 s in the lower panel. Accordingly, in Figure 11, we plot the data in the two bands against the time measured from the effective magnetic equator.

The shells are no longer symmetrical inbound and outbound using the new time coordinate. The D-ring crossings are shaded. Vertical dashed lines are shown separated by 175 s in the upper plot and 300 s in the lower. Below the time axis are listed not only EqL but also more information concerning the magnetic shell where the spacecraft is. The northern and southern ionospheric latitudes of the shell are listed, as is the latitude of the spacecraft. We will return to the significance of this ancillary information subsequently.

The color of the traces changes from red to blue at the innermost magnetic shell encountered i.e. at the point where the spacecraft motion changes from inbound across magnetic shells to outbound. The most important result from the change in time reference is that both low and high frequency signals now appear to have a magnetic node ($\Delta B_\phi{\sim}0$) close to the passage through the proxy magnetic equator. As shown in the theory discussion, if the signals we have found were simply $n = 1$ and 2 harmonics of standing Alfvén
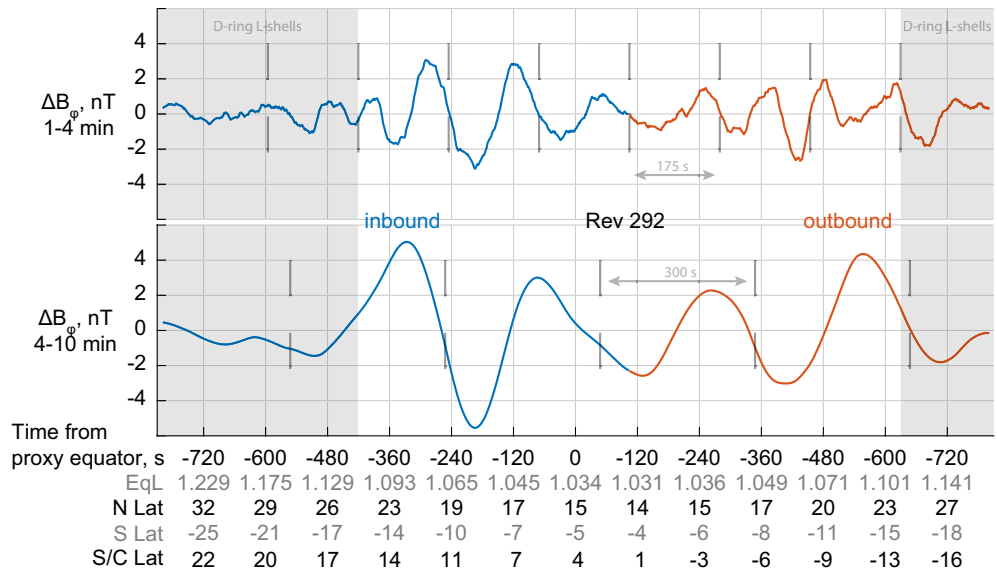
Figure 11. Azimuthal field B_ϕ from Rev 292 divided into two bands 1–4 min and 4–10 min by the spline subtraction and windowing procedure described in the text. Time is measured from the point where the planetary field is horizontal ($B_r = 0$), the proxy for the magnetic equator. It can be seen that both low and high frequency signals now appear to have a magnetic node ($\Delta B_\phi \sim 0$) close to the passage through the proxy magnetic equator. The traces in each panel are color coded; the color changes from blue to red where the spacecraft encounters the innermost magnetic shell. Where the spacecraft is on D-ring shells is shaded. Vertical dashed lines in the upper and lower panel are separated by 175 and 300 s respectively. Ancillary data: the parameter EqL (spacecraft magnetic shell), S/C Lat, the spacecraft latitude and the latitudes of the northern and southern feet of the field lines, N Lat, S Lat are given below the time axis.
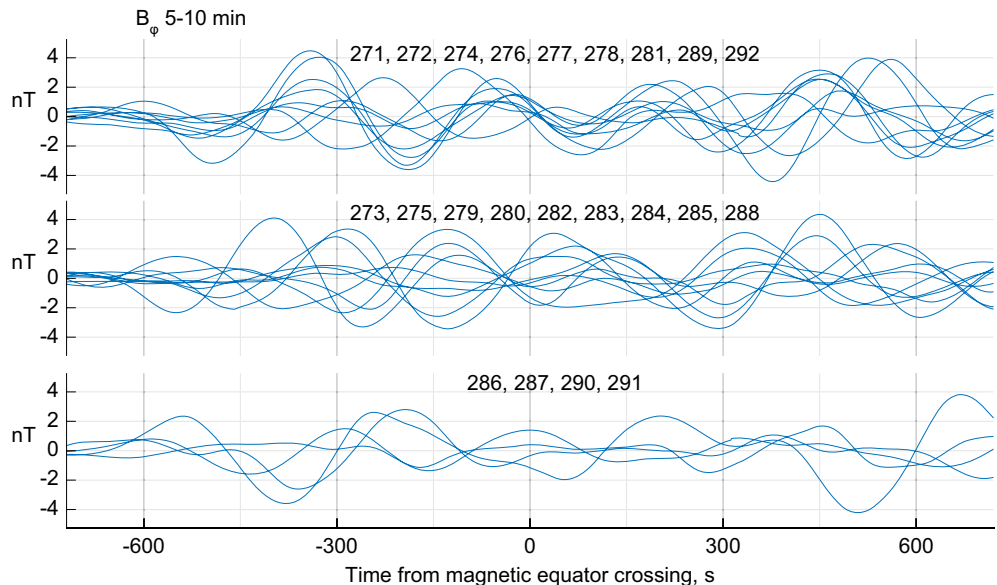
Figure 12. Azimuthal field ΔB_ϕ signals from the low frequency band [5–10 min]. On the x-axis, time, T, is measured in seconds from where the spacecraft crosses the proxy magnetic equator (where the background radial field, $B_r = 0$). Orbits are divided into three sets. The top panel shows ΔB_ϕ traces overlaid recorded on Revs 271, 272, 274, 276, 277, 278, 281, 289, and 292, the middle panel, Revs 273, 275. 279, 280, 282, 283, 284, 285, 288 and the bottom panel Revs 286, 287, 290, and 291. Traces in the top panel show a node between T = −6 and 35 s just after the equator crossing. In the middle panel, traces show a node between T = −30 and −40, just in advance of the proxy equator (background $B_r = 0$) crossing. The bottom panel contains traces from four orbits, Rev 286, 287, 290, 291, which appear anomalous in not fitting with the patterns in the other two sets.
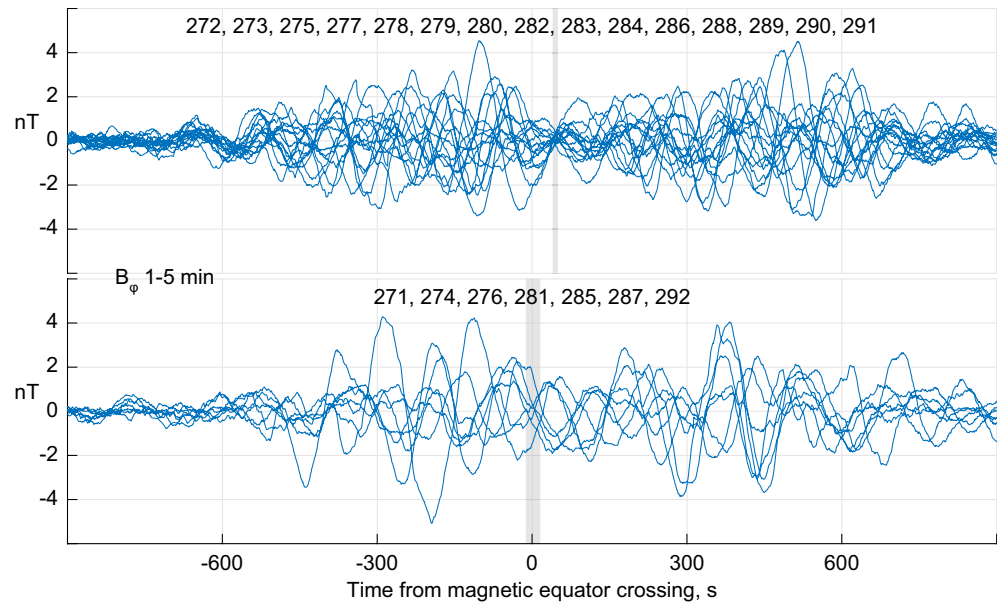
Figure 13. Azimuthal field signals from the higher frequency band. The x-axis is time, T, measured in seconds from the spacecraft crossing of the proxy equator (where the background radial field, $B_r = 0$). Orbits are divided into two sets. As in Figure 11, labels above each panel indicate the two groupings of passes: in the top panel Revs 272, 273, 275, 277, 278, 279, 280, 282, 283, 284, 286, 288, 289, 290 and 291 and a shaded vertical bar shows the location of a magnetic node between T = 40 and 50 s. The lower panel shows traces from Revs 271, 274, 276, 281, 285, 287 and 292. This group shows a clustering of nodes between T = −12 and +16 s. Shading indicates the location of the zeroes.

modes a node in one and an antinode in the other would be expected. The nodes detected in each signal on Rev 292 in Figure 10 show that this expectation is not borne out. In Figures 12 and 13, we show that this result is general.

In Figure 12 we take all the proximal orbit passes ordered by the time, T, from crossing the effective magnetic equator (defined by the background radial field being zero). The innermost magnetic shell encountered varies from 1.06 to 1.03. The time axis is marked with ticks 300 s apart. Inspection shows all traces show signals at around this period. The orbits in each panel are marked above the panel. The traces in the three panels exhibit three different types of behavior near T = 0 (background $B_r = 0$). The traces from Revs, 271, 272, 274, 276, 277, 278, 281, 289, and 292 are shown in the top panel. Zeroes occur in each trace within the range T = −6 and +35 s on each side of T = 0 where the spacecraft crosses the proxy magnetic equator (background $B_r = 0$). We shall interpret the zeroes as due to magnetic nodes, i.e. points where the wavefield does not vary. The second panel shows traces from Revs 273, 275. 279, 280, 282, 283, 284, 285, and 288. In this set the traces all show a magnetic node between T = −30 and −40 s before the spacecraft reaches the proxy magnetic equator at T = 0.

The lowest panel shows four exceptional cases. On Revs 286, 287, 290, and 291 the nearest nodes to T = 0 are between T = −110 and −90. Indeed, Rev 286 shows a local ΔB_ϕ maximum, that is, what could be an antinode, near T = 0. Although the amplitudes are small on Revs 287, 290, and 291 no trace shows a zero close to T = 0.

Apart from pointing out the likelihood of finding a magnetic node near the proxy magnetic equator, we have no explanation of the clustering. There seems no link to the depth of the orbit's penetration of magnetic shells. The deepest penetrating orbits are Rev 288–292. Two are in the top panel and one in the middle and two in the bottom panel of Figure 12. Nor is any relation to the Provan et al. (2019) classification of background very clear. The distinction between A and B categories is not clear if judged on the basis of our smoothed background (cf. the bottom panel of Figure 5). Of the five category U passes, one appears in the top panel, two in the middle panel and two in the bottom panel of Figure 12.
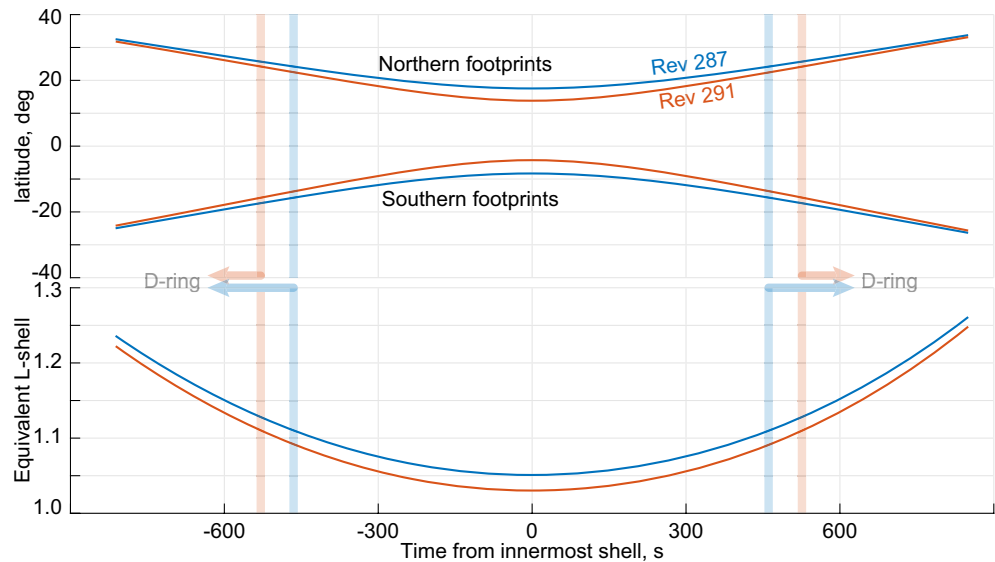
Figure 14. Plots versus time of the latitudes of northern and southern feet of the field passing through the Cassini orbit on Rev 287 (blue traces) and Rev 291 (red traces) (top panel) and Equivalent L shell (EqL) (bottom panel). Shading indicates where the spacecraft is on magnetic shells mapping to the D-ring. Time is measured from the time of encounter with innermost shell.

The high frequency signals for all orbits are shown in Figure 13. Once again, the y-axis labels the passes whose traces are shown in the panel. The top panel shows traces from 272, 273, 275, 277, 278, 279, 280, 282, 283, 284, 286, 288, 289, 290, and 291. In this panel the 15 traces all show a magnetic node between 40 and 50 s indicated by the shaded vertical bar after the crossing of the proxy magnetic equator ($B_r = 0$).

The lower panel shows traces from the remaining orbits, Revs 271, 274, 276, 281, 285, 287, and 292. The traces do not show the magnetic node between T = 40 and 50 s. Rather several of the traces are closer to showing an antinode at this time. However, the seven traces do show a clustering of nodes between T = −12 and 16 s close to the origin.

Overall, on all orbits the high frequency band signals had a magnetic node within 50 s of T = 0, the time of passage through the proxy magnetic equator and 15 (68%) showed nodes clustered within 5 s of T = 45 s.

6. Discussion

The variations detected in the azimuthal field component on times scales less than 10 min appear to be made up of standing Alfvén waves on the magnetic shells that are planetward of the D-ring at Saturn. They are not the simplest imaginable Alfvén waves, that is, harmonically related eigenmodes. This is despite the strong azimuthal polarization and the evidence that the spectrum might be separated into roughly harmonically related bands. The field guidance of a pure Alfvén mode means that its eigenfrequencies are controlled by the field line length and how the Alfvén speed varies along the field. We have only limited information on how the variation of Alfvén speed might vary along or across the field, but we do know how the field line length changes. The field lines between the crossing of the D-ring inner edge (EqL = 1.11) and the innermost shells encountered (1.03 < EqL < 1.06) vary little in the altitude attained (<1% of R_s). Nonetheless, the field line length changes substantially. In the ancillary data below Figure 11 we give the latitude where the shell on which the spacecraft is meets the ionosphere in each hemisphere. We present similar information graphically in Figure 14. The latitudes of the northern and southern field line feet in the ionosphere are shown for two orbits, Rev 287 (Minimum EqL = 1.06) (blue traces) has one of the shallowest periapses, and Rev 291 (Minimum EqL = 1.03), a deep penetrating orbit (red traces). At the inner edge of the D-ring the latitude range spanned by the field line passing through trajectories inbound and outbound is ~40°. At closest approach, the field line for Rev 287 spans 26° while the field at Rev 291 spans 18°. Thus, planetward of the D-ring shell the field line length varies by a factor of 2 for Rev 291 and by ~1.5 for Rev 287.
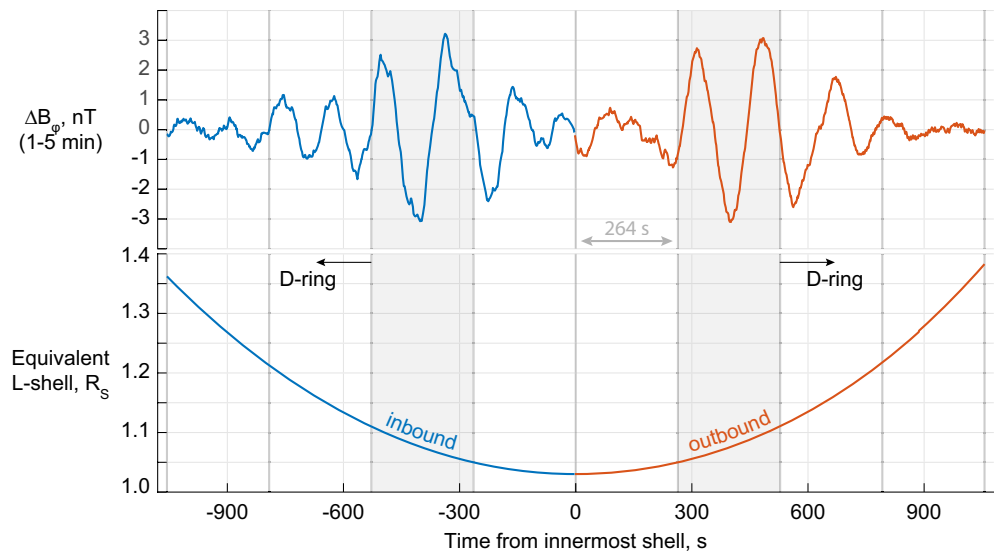
Figure 15. Azimuthal field signals from the 1–5 min band (top panel) and equivalent L shell, EqL for Rev 291. Trace color is red before innermost shell encounter and blue after. The x-axis in both panels is time, T, measured in seconds from when the spacecraft encounters the innermost magnetic shell (EqL = 1.03). More information on the Rev 291 background field lines is given in the red traces in Figure 14. The shaded regions correspond to when the spacecraft is crossing magnetic shells with 1.05 < EqL < 1.11 inbound (left) and outbound (right). The vertical lines are separated by 264 s. The magnetic shell at the D-ring inner edge is crossed at T = ±528 s.

In general, as the spacecraft reaches the magnetic shells corresponding to the D-ring planetward edge, the amplitude detected is often the largest encountered on the pass. This can be seen in the figures in this study. As the spacecraft, which is moving primarily north-south, crosses more than 30° of planetary latitude on even the shallowest encounter (Rev 287) with the waves, it seems fair to conclude that they occupy a large fraction of the field lines and are not confined for example to the equatorial region of the shells. Accordingly, the variation in field line length should lead to expectations of large variation of eigenfrequency.

We have no firm information to distinguish how plasma mass density varies along or across the field, but large local changes of ion mass density are detected by the Cassini Ion and Neutral Mass Spectrometer (Cravens et al., 2019). Even if the Alfvén speed were to vary little radially, the change in field line length would induce substantial changes in period. The spacecraft takes typically 450 s to move from the outermost to innermost shell. On Rev 292 (whose orbit is similar to Rev 291 data is shown in Figures 7 and 11) 450 s corresponds precisely to a period and a half of the signal in the lower panel of each figure. The amplitude decreases as the inner shells are approached but the period shows no apparent change despite the field line length increasing by a factor of 2. It seems thus likely that the period is not determined by the local field conditions alone.

Although the signals in both bands are usually not sinusoidal no obvious systematic dependence of period on magnetic shell has been detected. The conclusion can be drawn that the signals are not simply local oscillating field lines but rather some other source is determining the preferred periods (e.g., global modes as we discuss below). The local field line resonances are being pumped from that source.

We have already noted that there may be phase jumps in signals between northern and southern crossings of the same shells. Figure 15 shows an important example illustrating the magnetic shell structure of the signals. Happenstance is important in the case in question on Rev 291; the time taken by the spacecraft to travel between the points where amplitude peaks north and south is fortuitously three times the period.

ΔB_ϕ data from the 1–5 min windowed data on Rev 291 are shown in the top panel. As our interest is in the signal dependence on magnetic shell, we revert to plotting data against time from the innermost shell crossing. In the lower panel the magnetic shell parameter (EqL) is plotted for the same orbit. The symmetry of the EqL plot about the innermost shell at T = 0 means that it is straightforward to judge on a time plot when the spacecraft is on the same magnetic shells inbound and outbound. Shading indicates the region of interest where EqL is between 1.05 and 1.11 where the signal amplitudes peak.

The vertical markers in Figure 15 are separated by 264 s. The ranges inbound that are shaded contain 1.5 cycles of an oscillation whose period is apparently 176 s. The periodicity is less clear in the time range $-264 < T < 264$, where the spacecraft is approaching the innermost shells. By chance, the time taken for the spacecraft to traverse this range (528 s) corresponds to precisely three cycles ($528 = 3 \times 176$). Thus precisely three cycles have elapsed once the spacecraft returns to the same shells outbound. Signals might be expected to be in phase except that the spacecraft will also have moved from the northern hemisphere to the southern. Recalling that we have deduced that there is a magnetic node between hemispheres and the signals in the south should have a phase shift π with respect to the northern signals on the same shells. Comparing the signals outbound and inbound shows this is indeed the case. Indeed, the crossing of the magnetic equator is at $T = -103$ s. This corresponds to the first zero in ΔB_ϕ to the left of $T = 0$.

This result provides a rather direct confirmation that signals are ordered by magnetic shell but also confirms our hypothesis of standing wave structure with a node (i.e., sign change near the equator where the spacecraft moves from the northern hemisphere to south). However, the elegance of the relationship between inbound and outbound signals along a spacecraft trajectory required the happenstance that the time spent between inbound/outbound or northern/southern encounters with the shells where the Alfvén wave amplitudes peaks was a multiple of the period. This will not normally occur. There can be quite different phase changes between inbound and outbound crossing of the same shell. Moreover, the period needs to be very stable for unambiguous identification of the phase.

Although the signals in Figure 15 show many signs of being standing Alfvén waves, the spectrum seems too discrete for the signals to be simple local excitation. Nonetheless, even if the signals are pumped by a fairly narrow band source, features due to field line resonance are also expected to be found. The resonance width in frequency may depend on the bandwidth of the source, or on the local dissipation rate. The band width in the frequency domain also determines the radial scale of the signals. Moreover, a phase shift of π occurs in the ΔB_ϕ component across the resonant shell. For strong damping the resonance would be broad, spacecraft motion might be important and the shift might appear as a change in frequency in ΔB_ϕ (with respect to any oscillation detectable in the other directions) as the spacecraft moves through. This effect is probably present in Figure 3 where the signals from the Revs 290 and 291 change within a cycle from being close to out of phase to almost in phase and back. If the resonances are narrow and damping is weak, phase jumps would be abrupt and the ΔB_ϕ signal will show a sudden change of sign. In general, irregular phase behavior can be expected from the effects of field line resonance. However, more detailed modeling is needed to establish what can be securely identified. The nature of the data presented here, in particular, the capacity to separate oscillatory signals on different time scales by the windowed spline process, suggests we are not detecting simple excitation of all local field line resonances. That would produce a continuum of excited resonant shells. It is likely that although the field-line resonance effects (Southwood, 1974) are present, some further effect is selecting the particular frequencies excited. The most likely reason for the preferential frequencies is that their origin is in the global (fast mode) resonances of a much larger cavity or even the entire magnetosphere. Kivelson and Southwood (1985, 1986) and also Allan et al. (1986) suggested that coupling of global cavity fast modes might lead to Alfvén mode field line resonances at discrete frequencies. Kivelson and Southwood's original work, proposed that fast mode eigenmodes in the magnetospheric cavity would be inherently damped by a one-way transfer of energy to the magnetic shell where the fast eigenfrequency matched the field line resonance frequency. In practice, any excitation of the overall cavity will thus excite field line resonances only on those shells where global eigenfrequencies matched local resonances. The Kivelson and Southwood ideas have since been followed up and expanded in theory, simulation and used in explaining many observations in a terrestrial context by many authors (Allan et al., 1986; Bentley et al., 2018; Claudepierre et al., 2010, 2016; Elsden & Wright, 2019; Elsden et al., 2016; Hartinger et al., 2013, 2014; Inhester, 1987; Mann et al., 1995, 2002; Samson et al., 1992; Takahashi et al., 2018; Wright & Mann, 2006; Wright & Elsden, 2020).

7. Concluding Remarks

The Cassini spacecraft magnetometer detected azimuthally polarized oscillations during the proximal orbits about Saturn. The oscillations are superposed on the large scale azimuthal magnetic perturbations that have been studied by Khurana et al. (2018), Provan et al. (2019), and Hunt et al. (2019). The oscillatory signals are

present on all 22 proximal orbit passes and show a large amount of similarity from orbit to orbit, in contrast with the background disturbances.

We have argued that the signals appear to be mainly time domain signals in the frame of the background plasma. In particular, in specific instances we have shown that once the background signal with variations on a time scale greater than 10 min is removed, the residual signals may often be represented by the sum of two or three quasisinusoidal signals. In general, we have been able to separate signals into two bands, with periods of order 100–200 s and >300 s, respectively.

Signals in both bands show a magnetic node near where the spacecraft passes through what we have called the proxy magnetic equator (where the background field is horizontal, $B_r = 0$). There are only four exceptions out of 44 swathes.

The simplest theory would be that the spacecraft is flying through low order eigenmodes of the Alfvén mode. The standing structure would lead one to expect that odd modes would have a magnetic node near the background field equator and even modes would have an antinode there. Two features of the observations suggest that the actual situation is more complex. First, although the oscillation periods in the two bands might appear to be harmonically related with the longer period roughly double the shorter, both bands show a magnetic node near the field symmetry point meaning that they would all be odd harmonics ($n = 1$, 3, or 5) which seems unlikely.

Although the field line resonance frequencies vary with magnetic shell, yet we detect no immediate feature of the frequency variation with shell that one would expect with purely local Alfvén wave excitation. Accordingly, it seems more likely that the spectral content is set by coupling to fast mode eigenmodes of a larger volume of the dayside magnetosphere. Despite the lack of evidence of systematic variation of period with the magnetic shell, there are some aspects of the signals that could be associated with field line resonance. The periods detected on the spacecraft do vary. Moreover, the signals can show sudden phase jumps, as would be expected if the spacecraft were crossing a resonant shell.

It does appear that the oscillatory signals are always present and that the amplitude does not vary greatly from orbit to orbit. This suggests that the signals are not directly linked to the background B_ϕ, which is not only highly variable from orbit to orbit but also does not share the north-south symmetry we have found in the oscillatory signals.

We conclude that the final 22 proximal orbits took the Cassini spacecraft into a regime on magnetic shells planetward of the D-ring where standing Alfvén waves are always present. The signals appear to be particular local field line resonances being pumped by global magnetospheric cavity modes. The dominant ~150 and ~300 s periods detected throughout the proximal orbits thus would correspond to global (fast) mode eigenfrequencies. The existence of such global modes was originally suggested by Kivelson and Southwood (1985).

Data Availability Statement

The data used in this work are readily available from the NASA Planetary Data System, https://data.nasa.gov/Space-Science/Planetary-Data-System-PDS-/9epu-76zj.

References

Allan, W., White, S. P., & Poulter, E. M. (1986). Impulse-excited hydromagnetic cavity and field-line resonances in the magnetosphere. *Planetary and Space Science*, *34*, 371. https://doi.org/10.1016/0032-0633(86)90144-3

Bentley, S. N., Watt, C. E. J., Owens, M. J., & Rae, I. J. (2018). ULF wave activity in the magnetosphere: Resolving solar wind interdependencies to identify driving mechanisms. *Journal of Geophysical Research: Space Physics*, *123*(4), 2745–2771. https://doi.org/10.1002/2017JA024740

Cao, H., Dougherty, M. K., Hunt, G. J., Provan, G., Cowley, S. W. H., Bunce, E. J., et al. (2019). The landscape of Saturn's internal magnetic field from the Cassini Grand Finale. *Icarus*, *244*, e113541. https://doi.org/10.1016/j.icarus.2019.113541

Claudepierre, S. G., Hudson, M. K., Lotko, W., Lyon, J. G., & Denton, R. E. (2010). Solar wind driving of magnetospheric ULF waves: Field line resonances driven by dynamic pressure fluctuations. *Journal of Geophysical Research*, *115*, A11202. https://doi.org/10.1029/2010JA015399

Claudepierre, S. G., Toffoletto, F. R., & Wiltberger, M. (2016). Global MHD modeling of resonant ULF waves: Simulations with and without a plasmasphere. *Journal of Geophysical Research: Space Physics*, *121*, 227–244. https://doi.org/10.1002/2015JA022048

Cravens, T. E., Moore, L., Waite, J. H., Jr, Perryman, R., Perry, M., Wahlund, J.-E., et al. (2019). The ion composition of Saturn's equatorial ionosphere as observed by Cassini. *Geophysical Research Letters*, *46*, 6315–6321. https://doi.org/10.1029/2018GL077868

Dougherty, M. K., Cao, H., Khurana, K. K., Hunt, G. J., Provan, G., Kellock, S., et al. (2018). Saturn's magnetic field revealed by the Cassini Grand Finale. *Science*, *362*, eaat5434. https://doi.org/10.1126/science.aat5434

Elsden, T., & Wright, A. N. (2019). The effect of fast normal mode structure and magnetopause forcing on FLRs in a 3-D waveguide. *Journal of Geophysical Research: Space Physics*, *124*, 178–196. https://doi.org/10.1029/2018JA026222

Elsden, T., Wright, A. N., & Hartinger, M. D. (2016). Deciphering satellite observations of compressional ULF waveguide modes. *Journal of Geophysical Research: Space Physics*, *121*, 3381–3394. https://doi.org/10.1002/2016JA022351

Hartinger, M. D., Angelopoulos, V., Moldwin, M. B., Takahashi, K., & Clausen, L. B. N. (2013). Statistical study of globalmodes outside the plasmasphere. *Journal of Geophysical Research: Space Physics*, *118*, 804–822. https://doi.org/10.1002/jgra.50140

Hartinger, M. D., Welling, D., Viall, N. M., Moldwin, M. B., & Ridley, A. (2014). The effect of magnetopause motion on fast mode resonance. *Journal of Geophysical Research: Space Physics*, *119*, 8212–8227. https://doi.org/10.1002/2014JA020401

Hunt, G. J., Cowley, S. W. H., Provan, G., Cao, H., Bunce, E. J., Dougherty, M. K., & Southwood, D. J. (2019). Currents associated with Saturn's intra-D-ring azimuthal field perturbations. *Journal of Geophysical Research: Space Physics*, *124*(7), 5675–5691. https://doi.org/10.1029/2019JA026588

Inhester, B. (1987). Numerical modeling of hydromagnetic wave coupling in the magnetosphere. *Journal of Geophysical Research*, *92*, 4751–4756. https://doi.org/10.1029/JA092iA05p04751

Khurana, K. K., Dougherty, M. K., Provan, G., Hunt, G. J., Kivelson, M. G., Cowley, S. W. H., et al. (2018). Discovery of atmospheric-wind-driven electric currents in Saturn's magnetosphere in the gap between Saturn and its rings. *Geophysical Research Letters*, *45*(10), 10068–10074. https://doi.org/10.1029/2018GL078256

Kivelson, M. G., & Southwood, D. J. (1985). Resonant ULF waves: a new interpretation. *Geophysical Research Letters*, *12*, 49. https://doi.org/10.1029/gl012i001p00049

Kivelson, M. G., & Southwood, D. J. (1986). Coupling of global magnetospheric MHD eigenmodes to field line resonances. *Journal of Geophysical Research*, *91*, 4345. https://doi.org/10.1029/ja091ia04p04345

Mann, I. R., Voronkov, I., Dunlop, M., Donovan, E., Yeoman, T. K., Milling, D. K., et al. (2002). Coordinated ground-based and cluster observations of large amplitude global magnetospheric oscillations during a fast solar wind speed interval. *Annales Geophysicae*, *20*(4), 405–426. https://doi.org/10.5194/angeo-20-405-2002

Mann, I. R., Wright, A. N., & Cally, P. S. (1995). Coupling of magnetospheric cavity modes to field line resonances: A study of resonance widths. *Journal of Geophysical Research*, *100*(A10), 19441. https://doi.org/10.1029/95ja00820

Provan, G., Cowley, S. W. H., Bunce, E. J., Bradley, T. J., Hunt, G. J., Cao, H., et al. (2019). Variability of intra–D-ring azimuthal magnetic field profiles observed on Cassini's proximal periapsis passes. *Journal of Geophysical Research: Space Physics*, *124*(1), 379–404. https://doi.org/10.1029/2018JA026121

Samson, J. C., Harrold, B. G., Ruohoniemi, J. M., & Walker, A. D. M. (1992). Field line resonances associated with MHD waveguides in the magnetosphere. *Geophysical Research Letters*, *19*, 441–444. https://doi.org/10.1029/92gl00116

Southwood, D. J. (1974). Some features of field line resonances in the magnetosphere. *Planetary Space Science*, *22*, 483. https://doi.org/10.1016/0032-0633(74)90078-6

Takahashi, K., Lysak, R., Vellante, M., Kletzing, C. A., Hartinger, M. D., & Smith, C. W. (2018). Observation and numerical simulation of cavity mode oscillations excited by an interplanetary shock. *Journal of Geophysical Research: Space Physics*, *123*(3), 1969–1988. https://doi.org/10.1002/2017JA024639

Wright, A. N., & Elsden, T. W. (2016). Theoretical foundation of 3D Alfvén resonances : normal modes. *The Astrophysical Journal*, *833*(2), 1–10. https://doi.org/10.3847/1538-4357/833/2/230

Wright, A. N., & Elsden, T. (2020). Simulations of MHD wave propagation and coupling in a 3-D magnetosphere. *Journal of Geophysical Research: Space Physics*, *125*, e2019JA027589. https://doi.org/10.1029/2019JA027589

Wright, A. N., & Mann, I. R. (2006). Global MHD eigenmodes of the outer magnetosphere. In Takahashi, K., Chi, P., Denton, R. E. & Lysak, R. L. (Eds.), *Magnetospheric ULF waves: Synthesis and new directions, geophysical monograph series* (Vol. *169*, pp. 51–72). Washington, DC: American Geophysical Union. https://doi.org/10.1029/169GM06